Structure and phase transitions in $0.5(Ba_{0.7}Ca_{0.3}TiO_3)$-$0.5(BaZr_{0.2}Ti_{0.8}O_3)$ from -100 °C to 150 °C

Astri Bjørnetun Haugen,[1,a)] Jennifer S. Forrester,[2] Dragan Damjanovic,[3] Binzhi Li,[4] Keith J. Bowman,[5] and Jacob L. Jones [2,b)]

[1]Department of Materials Science and Engineering, Norwegian University of Science and Technology, 7491 Trondheim, Norway

[2]Department of Materials Science and Engineering, University of Florida, Gainesville, Florida 32611, USA

[3]Swiss Federal Institute of Technology – EPFL, 1015 Lausanne, Switzerland

[4]Department of Chemical Engineering and Materials Science, University of California-Davis, Davis, California 95616, USA

[5]Armour College of Engineering, Illinois Institute of Technology, Chicago, Illinois 60616, USA

[a)] This work was conducted while the author was visiting the University of Florida

[b)]Author to whom correspondence should be addressed. Electronic mail: jjones@mse.ufl.edu

ABSTRACT

The solid solution of $(x)Ba_{0.7}Ca_{0.3}TiO_3 - (1-x)BaZr_{0.2}Ti_{0.8}O_3$ is known to exhibit high piezoelectric constants. Discrepancies in the reported phase transitions and structure around room temperature, however, have complicated the understanding of the enhanced properties. Rietveld refinement of high-resolution X-ray diffraction is employed here to establish and refine the crystallographic structure at temperatures from -100 °C to 150 °C for x=0.5. A combination of rhombohedral *R*3*m* and tetragonal *P*4*mm* is found to coexist at temperatures of 20 °C and -25 °C, bordered by single phase rhombohedral and tetragonal regions at lower (i.e., -100 °C) and higher (i.e., 70 °C) temperatures, respectively. The diffractograms also show signs of strain and domain wall scattering that are linked to the sample history.

I. INTRODUCTION

The properties of ferroelectric compositions near morphotropic phase boundaries (MPBs) and polymorphic phase transitions (PPTs) are often superior to compositions far from these boundaries. Thus, the identification of phase transitions in ferroelectric solid solutions is of high relevance to identifying useful compositions. The $(x)Ba_{0.7}Ca_{0.3}TiO_3–(1-x)BaZr_{0.2}Ti_{0.8}O_3$ (100(1-x)BZT-100xBCT) solid solution was recently shown by Liu and Ren[1] to exhibit very high room-temperature piezoelectric coefficients of up to 620 pC/N. A phase diagram based on X-ray diffraction (XRD) measurements and dielectric spectroscopy was proposed that included cubic, tetragonal, and rhombohedral phases (Fig. 1(a)). The enhanced piezoelectric performance has been attributed to vanishing polarization anisotropy and polarization rotation in the presence of a tricritical point.[1] For 50BZT-50BCT, the phase transition sequence upon decreasing temperature was originally proposed as cubic, tetragonal, then rhombohedral. Further investigation of the microstructure by transmission electron microscopy has revealed the coexistence of tetragonal and rhombohedral nanodomains around the MPB, a microstructure commonly associated with high piezoelectric performance.[2] Recent work has also reported the room temperature structure as mixed-phase rhombohedral and tetragonal.[3] The parent phase $BaTiO_3$ has an intermediate orthorhombic phase at temperatures between the tetragonal and rhombohedral phases, a fact which has also motivated reports that 50BZT-50BCT is mixed-phase rhombohedral and orthorhombic at room temperature.[4,5] However, no orthorhombic crystallographic model has yet been shown to describe the data.[4,5]

Property measurements also suggest the possibility of extra phase transitions, in addition to the expected cubic-tetragonal and tetragonal-rhombohedral transitions for 50BZT-50BCT. For example, Benabdallah *et al.*[6] observed peaks in the pyroelectric current at 93 °C, 25 °C and -3 °C, and Damjanovic *et al.*[7] reported anomalies in dielectric and elastic

properties at approximately 90 °C, 34 °C, 8 °C and -60 °C (Fig. 1(b)). Thus, further crystallographic characterization of the BZT-BCT system and interpretation relative to the property coefficients is needed to more fully understand the phase diagram and properties.

In materials containing multiple polymorphic phases and overlapping reflections, analysis of subtle structural differences using XRD requires high resolution and low instrumental contributions to peak broadening. Analysis of higher 2θ reflections is preferred to resolve subtle peak splitting, but doing so requires very high intensity X-ray sources to compensate for the lower intensity. Therefore, high-resolution powder diffraction data were recorded in this study at a synchrotron X-ray source in order to investigate the phase sequence in the composition 50BZT-50BCT from -100 °C to 150 °C. Crystallographic structure refinement using the Rietveld method was applied to resolve the structure at selected temperatures.

II. EXPERIMENTAL

Powder used in this investigation was produced by mixing high purity $BaCO_3$ (99.95%), $CaCO_3$ (99%), TiO_2 (99.8%), and $BaZrO_3$ (99.5%) powders (Sigma Aldrich) followed by calcining at 1350 °C for 2 h to produce uniform composition powders.[8] The powders were uniaxially pressed into disks and ceramic samples were obtained by sintering powder disks at 1450 °C. Sintered ceramic samples were crushed into powders again, and high-resolution powder XRD patterns were measured at beamline 11-BM at the Advanced Photon Source, Argonne National Laboratory. The powder was loaded into a 0.4 mm quartz capillary, mounted in the beam-path and rotated continuously to enhance powder or orientation averaging.

Diffraction patterns were recorded in the temperature range -100 °C to 150 °C; the temperature was controlled by an Oxford Cryostream 700+ N_2 gas blower. For the applied

measurement energy, the calibrated wavelength was 0.412953 Å and the resolution $\Delta Q/Q = 1.7\times10^{-4}$, corresponding to an instrumental contribution to the peak full width at half maximum of 0.005°.[9] Simultaneous high-resolution and high-speed data collection was obtained by use of a state-of-the-art scintillator-based multi-analyzer detector system.[10] Diffraction patterns were recorded using a 2θ range of 0.5° to 51° in 0.001° steps and a 0.1 s counting time at each step. A diffraction pattern was recorded at constant temperatures of 20 °C and 150 °C prior to cooling the sample to -100 °C and recording a sequence of patterns at incrementally increasing temperatures of -100 °C, -25 °C, 20 °C, 70 °C, 100 °C, and 120 °C. Rietveld refinements were performed using the GSAS software[11] with the graphical interface EXPGUI.[12] Refined parameters included the lattice parameters, atomic positions, isotropic atomic displacement parameters (U_{iso}), site occupancy, 2θ zero offset, intensity scale factor, profile shape parameters, and background. The background was refined with a shifted Chebyschev model utilizing 16 polynomial parameters (to account for contributions at low 2θ angle from amorphous silicone-based grease). Profile function 3, a pseudo-Voigt function with the Finger *et al.*[13] axial divergence correction, was employed for the refinement of cubic phases. Profile function 4, which includes Stephens' model for anisotropic micro-strain broadening,[14] was used to model the more asymmetric peak-shapes in the lower-temperature patterns. A-site atoms (Ba and Ca) were constrained to the origin and equivalent isotropic displacements. The B-site atoms (Ti and Zr) were constrained to the same atomic position and isotropic displacements.

Space groups and starting values for lattice parameters and atomic positions were obtained from the literature,[15,16] except for mixed phase patterns where refined parameters from neighboring temperatures were used as starting values. For the 20 °C pattern, a critical step was required in the routine in order to avoid a false minimum solution. This step was the exclusion of the pseudo-cubic (110)-type reflections (hereafter referred to as $(110)_{pc}$

reflections) from the fit during the initial stage of the refinement. Without exclusion, this group of reflections dominates the refinement because of its high intensity, yet it has low resolution of the structural distortions because of its low diffraction angle. Because of the large number of reflections in refinements containing multiple phases, initial values of lattice parameters were adjusted manually to fit the higher order reflections at higher angles (e.g., $(222)_{pc}$, $(400)_{pc}$ etc.), where peak splitting of subtle distortions is more clear. Phase fractions, atomic positions, isotropic displacements and profile parameters were refined first. Then lattice parameters were included in the refinement, before the $(110)_{pc}$ reflections were re-introduced, and the entire pattern refined.

III. RESULTS AND DISCUSSION

All major reflections can be indexed to a perovskite structure, with a gradual change in peak shape with temperature, as shown in Fig. 2 for selected reflections. The patterns measured at 100 °C, 120 °C and 150 °C appear consistent with the cubic space group $Pm\bar{3}m$ and were refined within this space group. At 70 °C the structure was refined to the tetragonal space group *P*4*mm*.

The 20 °C pattern recorded during the heating sequence was fit to a combination of *P*4*mm* and the rhombohedral space group *R*3*m*, converging at an R_p value of 5.0%. Using an SZMV calculation,[17] the phase fractions were found to be 58 wt% *R*3*m* and 42 wt% *P*4*mm.* Refinement to pure *P*4*mm* only resulted in an R_p value of 8.9%. Selected reflections refined using both models are shown in Fig. 3. This result demonstrates that a phase combination at 20 °C better qualitatively describes the measured diffraction pattern than a single phase refinement. Refinement using the orthorhombic space group *Amm*2 was also performed, but the experimental relative intensities could not be accounted for, and the refinement converged to an R_p value of 7.7%, higher than that obtained using the combined *R*3*m* and *P*4*mm* phases.

Including the space group *R*3*m* with *Amm*2 in a two-phase refinement did not result in a stable refinement. These results suggest that the orthorhombic phase is not present in this composition at these temperatures, in contrast to what has been proposed in Refs. 4 and 5.

The *R*3*m* phase in the 20 °C pattern refined to significantly broader peaks than the *P*4*mm* phase (see Fig. S1, supplementary information[18]). Constraining the width of the *R*3*m* phase to equal that of the *P*4*mm* phase (on the assumption that the microstructural contributions to broadening in the two phases are not significantly different) reduced the quality of the fit drastically. The refinement (shown in Fig. 4(a)) converged at an R_p value of 7.0% and a phase fraction of 23 wt% *R*3*m*. Because neither of these extremes (i.e., constrained or un-constrained broadening of each respective phase) is more justified than the other, we consider that the real phase fraction of the *R*3*m* phase at 20 °C is between 23 wt% and 58 wt%.

The sample history effect is also evident by comparing the two distinct diffraction patterns measured at 20 °C, both prior to and during the heating sequence. The intensity of the $(h00)_{pc}$ reflections, as shown for $(400)_{pc}$ in Fig. 4(b), is clearly dependent on thermal history as also shown by Ehmke *et al.*[3] In the present case, the differences are mostly observed as changes in peak broadening and diffuse scattering between the peaks. These changes can be ascribed to differences in domain wall scattering in the tetragonal phase, and/or microstrain in the rhombohedral phase.

The best refinement of the -25 °C pattern was also obtained by a combination of *P*4*mm* and *R*3*m* phases. The refinement converged at an R_p value of 4.9% with 5 wt% *P*4*mm* and 95 wt% *R*3*m* phase fractions. Due to the small fraction of *P*4*mm* phase, the lattice and profile parameters were the only parameters of this phase that were refined. Refinement with a pure *R*3*m* phase converged to an R_p value of 6.8% with a significantly poorer visual fit that

did not account for the asymmetry of the $(h00)_{pc}$ reflections. Selected reflections from both refinements at -25 °C are shown in Fig. 5.

The pattern at -100 °C was modeled by a single phase in the *R*3*m* space group. Possible indications of peaks in addition to the *R*3*m* peaks were observed as peak asymmetries or subtle shoulders on the high-angle $(222)_{pc}$ and $(133)_{pc}$ reflections, and refinement within the monoclinic *Cm* space group was therefore also attempted. However, the extra reflections allowed by symmetry lowering did not account for these possible profile deviations or otherwise improve the quality of the fit.

Final refined values at each temperature are listed in Table I. Additional refined values (atomic positions and isotropic displacement parameters) are listed in Table S.I (supplementary information[18]). All of the final refinements converged to R_p values of 6% or less. Fig. 6 shows some trends of the refined values as a function of temperature. Specifically, the rhombohedral and tetragonal spontaneous lattice strains appear to decrease with temperature while the average unit cell volume increases. These changes are expected because spontaneous ferroelastic lattice strains typically decrease with temperature and the coefficient of thermal expansion implies a unit cell volume increase. The phase sequence described in Fig. 6 is in good correlation with the gradual peak shape changes in the diffractograms (Fig. 3), and supports prior observations of a rhombohedral and tetragonal co-existence in the 50BZT-50BCT composition near room temperature.[2,3] The present work indicates that the two-phase coexistence region extends to temperatures down to 50 °C below room temperature, or at least to -25 °C.

The property measurements from Damjanovic *et al.*[7] that are re-drawn in Fig. 1(b) indicate three dominant phase transitions at approximately 90 °C, 34 °C and -60 °C. The phase transition at -60 °C was observed in Ref. 7 as both an inflection in the dielectric loss and a change in the Raman spectra that indicated a phase transition. In the present work, this

transition is attributed as a change between single-phase *R*3*m* at lower temperatures to mixed-phase *R*3*m* + *P*4*mm* at higher temperatures. Similarly, the transition around 34 °C in Ref. 7 is assigned from results in the present work as a transition from mixed-phase *R*3*m* + *P*4*mm* at lower temperatures to single-phase *P*4*mm* at higher temperatures. Finally, the transition at 90 °C in Ref. 7 is assigned from results in the present work as a transition from *P*4*mm* to $Pm3m$. The inflections in the dielectric and elastic properties around 8 °C however, cannot be attributed to a measurable phase transition from high-resolution X-ray diffraction. In the present work, the diffraction patterns measured at temperatures both below -25 °C and above 20 °C show differences that are best explained by changes in phase fractions, not by changes in the symmetry of the respective phases. It was observed that the phase fraction of *R*3*m* in this two-phase mixture changes from 95 wt% at -25 °C to somewhere between 23 wt% to 58 wt% at 20 °C. Most significantly, there were no observed superlattice reflections at either temperature that might be attributed to long-range octahedral tilting or other superstructure effects, and other phase combinations or phases of lower symmetry were not found to better describe the diffraction patterns. If a significant structural change exists in this temperature range, its signature in the diffraction pattern is small.

One remaining explanation that could describe the origin of the elastic and dielectric property inflections at 8 °C is that of domain wall motion. Domain wall motion can lead to inflections in property coefficients as has been shown, for example, in Refs. 19 and 20. The present results suggest that domain wall motion of either phase may be contributing to this property inflection and/or their coordinated effects and the temperature dependent phase changes suggest interphase boundary motion effects[21] may also be relevant. Other theories relating extrinsic mechanisms to piezoelectric and elastic properties have been discussed by Dong *et al.*[22] for $Ba(Zr,Ti)O_3$, though are mostly attributed to compositional inhomogeneity and the associated cooperative effects of different localized Zr-rich and Ti-rich regions.

While the present work cannot definitively ascribe these property anomalies to a particular mechanism, it presents evidence related to changing phase fractions that may support these developing theories.

The present results also inform the developing phase diagram of BCT-BZT. Both Ehmke *et al.*[3] and Yang *et al.*[5] recently suggested phase diagrams of BCT-BZT. As discussed previously, the diagram proposed by Yang *et al.*[5] includes an orthorhombic phase, yet an orthorhombic phase could not be found to adequately describe the high-resolution XRD patterns. The diagram by Ehmke *et al.*[3] proposes a region of rhombohedral and tetragonal phase coexistence near room temperature for 50BZT-50BCT. The present results further define the existence of this region in at least the range -25 °C to 20 °C and support this proposed phase diagram in that the structure is *R*3*m* at temperatures as low as -100 °C. Moreover, the present work suggests changing phase fractions within this region and preliminarily assigns quantitative phase fractions using the Rietveld method.

IV. CONCLUSION

A phase sequence has been established for 50BZT-50BCT from -100 °C to 150 °C by crystallographic refinement using the Rietveld method. High-resolution X-ray diffraction patterns allowed for a delineation of 50BZT-50BCT into cubic, tetragonal, tetragonal + rhombohedral and rhombohedral regions upon cooling. In the mixed-phase region, the phase fractions were quantified to 23-58 wt% *R*3*m* at 20 °C and 95 wt% *R*3*m* at -25 °C. This work agrees with the previously reported room temperature two-phase region and expands its range in temperature to well below room temperature. Contributions from domain wall scattering and/or microstructural strain dependent on thermal history are evident in the diffractograms.

ACKNOWLEDGEMENTS

J.J. and J.F. acknowledge partial support for this work from the U.S. Department of the Army under W911NF-09-1-0435, and J.J. acknowledges partial support for this work from the U.S. National Science Foundation (NSF) under award numbers DMR-0746902 and OISE-0755170. A.B.H. acknowledges financial support from the Norwegian University of Science and Technology. B. L. and K. B. were supported under NSF DMR-0805022. D.D. acknowledges financial support of FNS PNR62 Project No. 406240-126091. Use of the Advanced Photon Source at Argonne National Laboratory was supported by the U. S. Department of Energy, Office of Science, Office of Basic Energy Sciences, under Contract No. DE-AC02-06CH11357. The authors would like to thank Lyndsey Denis and Matthew Suchomel for help with data collection and Pam Thomas for helpful discussions.

REFERENCES

[1] W. F. Liu and X. B. Ren, Phys. Rev. Lett. **103**, 257602 (2009).

[2] J. H. Gao, D. H. Xue, Y. Wang, D. Wang, L. X. Zhang, H. J. Wu, S. W. Guo, H. X. Bao, C. Zhou, W. F. Liu, S. Hou, G. Xiao, and X. B. Ren, Appl. Phys. Lett. **99**, 092901 (2011).

[3] M. C. Ehmke, S. N. Ehrlich, J. E. Blendell, and K. J. Bowman, J. Appl. Phys. **111**, 124110 (2012).

[4] W. Li, Z. Xu, R. Chu, P. Fu, and G. Zang, Physica B **405**, 4513 (2010).

[5] Yang, Tian, Chai, Wei, and Liu, "Phase transition behavior and large piezoelectricity near morphotropic phase boundary of lead-free $(Ba_{0.85}Ca_{0.15})(Zr_{0.1}Ti_{0.9})O_3$ ceramics" J. Am. Ceram. Soc. (in press - early view; DOI 10.1111/jace.12049)

[6] F. Benabdallah, A. Simon, H. Khemakhem, C. Elissalde, and M. Maglione, J. Appl. Phys. **109**, 124116 (2011).

[7] D. Damjanovic, A. Biancoli, L. Batooli, A. Vahabzadeh, and J. Trodahl, Appl. Phys. Lett. **100**, 192907 (2012).

[8] B. Li, J. E. Blendell, and K. J. Bowman, J. Am. Ceram. Soc. **94**, 3192 (2011).

[9] J. Wang, B. H. Toby, P. L. Lee, L. Ribaud, S. M. Antao, C. Kurtz, M. Ramanathan, R. B. Von Dreele, and M. A. Beno, Rev. Sci. Instrum. **79**, 085105 (2008).

[10] P. L. Lee, D. Shu, M. Ramanathan, C. Preissner, J. Wang, M. A. Beno, R. B. Von Dreele, L. Ribaud, C. Kurtz, S. M. Antao, X. Jiao, and B. H. Toby, J. Synchrotron Radiat. **15**, 427 (2008).

[11] A. C. Larson and R. B. Von Dreele, Los Alamos National Laboratory Report LAUR 86-748, 2004 (unpublished).

[12] B. H. Toby, J. Appl. Crystallogr. **34**, 210 (2001).

[13] L. W. Finger, D. E. Cox, and A. P. Jephcoat, J. Appl. Crystallogr. **27**, 892 (1994).

[14] P. Stephens, J. Appl. Crystallogr. **32**, 281 (1999).

[15] R. H. Buttner and E. N. Maslen, Acta Crystallogr. B **48**, 764 (1992).

[16] G. H. Kwei, A. C. Lawson, S. J. L. Billinge, and S. W. Cheong, J. Phys. Chem.-US. **97**, 2368 (1993).

[17] R. J. Hill and C. J. Howard, J. Appl. Crystallogr. **20**, 467 (1987).

[18] See supplementary material at [URL will be inserted by AIP] for more detailed refinement output in Figs. S1-S4 and Table SI.

[19] B. L. Cheng, M. Gabbay, and G. Fantozzi, J. Mater. Sci. **31**, 4141 (1996).

[20] E. M. Bourim, H. Tanaka, M. Gabbay, G. Fantozzi, and B. L. Cheng, J. Appl. Phys. **91**, 6662 (2002).

[21] J. L. Jones, E. Aksel, G. Tutuncu, T.-M. Usher, J. Chen, X. Xing, and A. J. Studer, Phys. Rev. B **86**, 024104 (2012).

[22] L. Dong, D. S. Stone, and R. S. Lakes, J. Appl. Phys. **111**, 084107 (2012).

FIGURE AND TABLE CAPTIONS

FIG. 1. a) BZT-BCT phase diagram re-drawn from Liu and Ren[1], and b) possible phase transitions in 50BZT-50BCT as observed by Damjanovic *et al.*[7]

FIG. 2. Selected high-angle reflections of 50BZT-50BCT as recorded by high-resolution X-ray diffraction.

FIG. 3. The best fits of selected high-angle reflections in Rietveld refinements of 50BZT-50BCT at 20 °C using a) mixed-phase *R*3*m* + *P*4*mm* and b) single-phase *P*4*mm*.

FIG. 4. a) The best fits of selected high-angle reflections in Rietveld refinements of 50BZT-50BCT at 20 °C using mixed-phase *R*3*m* + *P*4*mm* with constrained peak widths. b) Diffraction patterns of 50BZT-50BCT recorded at 20 °C both prior to (dotted lines) and during (solid lines) the thermal sequence.

FIG. 5. Rietveld refinements of 50BZT-50BCT at -25 °C shown on selected reflections for a) *R*3*m* + *P*4*mm* and b) *P*4*mm*.

FIG. 6. Thermal trends in refined parameters of 50BZT-50BCT. a) Refined values for the rhombohedral angle α and tetragonality (c/a), b) refined unit cell volumes. The error bars are smaller than the symbol size. Grey areas indicate approximate phase transition temperatures.

TABLE I. Parameters from the best Rietveld refinement at each temperature for 50BZT-50BCT.

FIGURES AND TABLES

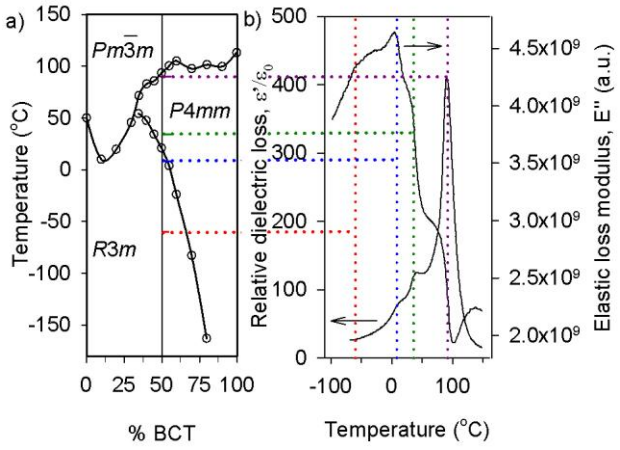

FIG. 1. a) BZT-BCT phase diagram re-drawn from Liu and Ren[1], and b) possible phase transitions in 50BZT-50BCT as observed by Damjanovic *et al.*[7]

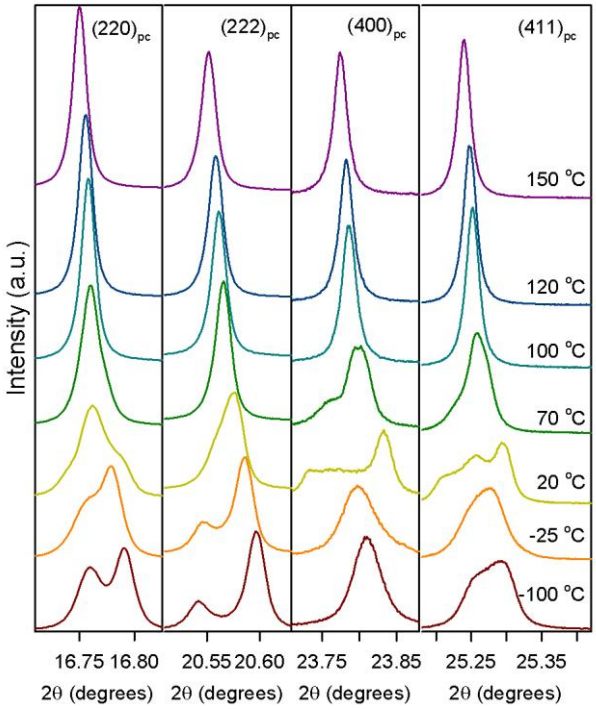

FIG. 2. Selected high-angle reflections of 50BZT-50BCT recorded by high-resolution X-ray diffraction.

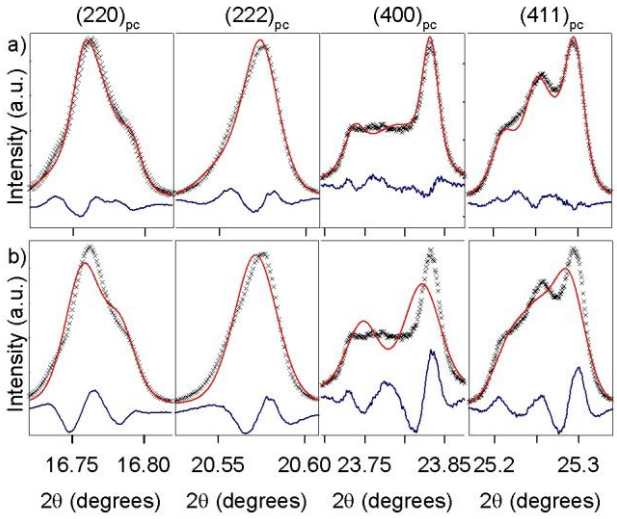

FIG. 3. The best fits of selected high-angle reflections in Rietveld refinements of 50BZT-50BCT at 20 °C using a) mixed-phase *R*3*m* + *P*4*mm* and b) single-phase *P*4*mm*.

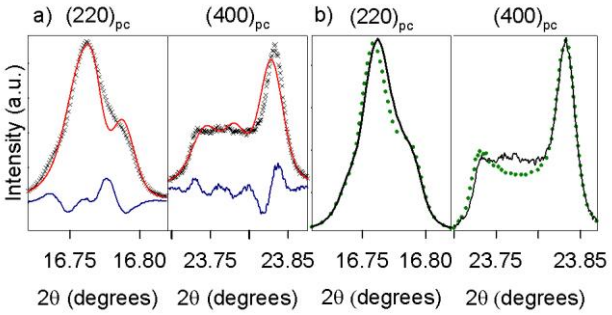

FIG. 4. a) The best fits of selected high-angle reflections in Rietveld refinements of 50BZT-50BCT at 20 °C using mixed-phase *R*3*m* + *P*4*mm* with constrained peak widths. b) Diffraction patterns of 50BZT-50BCT recorded at 20 °C both prior to (dotted lines) and during (solid lines) the thermal sequence.

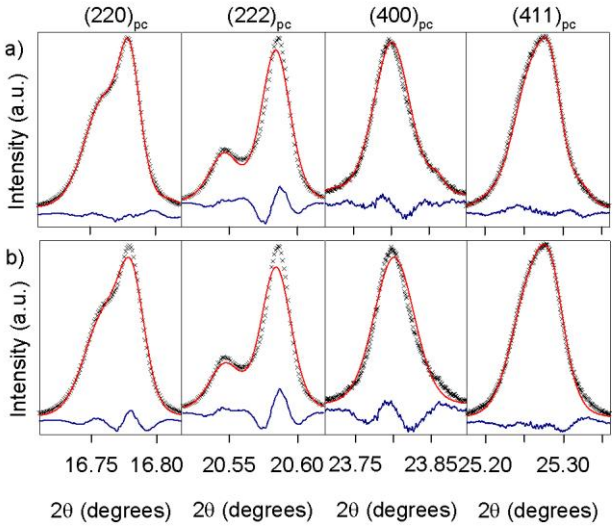

FIG. 5. Rietveld refinements of 50BZT-50BCT at -25 °C shown on selected reflections for a) *R*3*m* + *P*4*mm*, and b) *P*4*mm*.

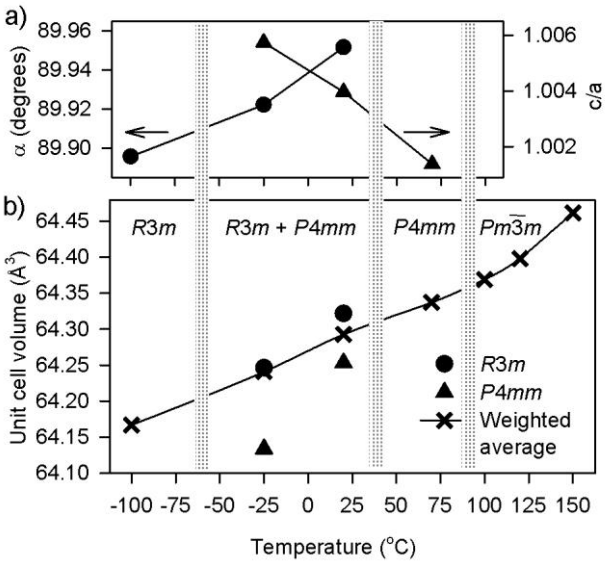

FIG. 6. Thermal trends in refined parameters of 50BZT-50BCT. a) Refined values for the rhombohedral angle α and tetragonality (c/a), b) refined unit cell volumes. The error bars are smaller than the symbol size. Grey areas indicate approximate phase transition temperatures.

TABLE I. Parameters from the best Rietveld refinement at each temperature for 50BZT-50BCT.

T (°C)	**Space group**	**Phase (wt%)**	**Lattice param. (Å or degrees)**	**Quality of fit**
150	$Pm\bar{3}m$	100	a = 4.009596(4)	R_p = 5.6% R_{wp} = 8.2% Chi^2 = 6.0
120	$Pm\bar{3}m$	100	a = 4.008277(4)	R_p = 5.6% R_{wp} = 7.9% Chi^2 = 5.6
100	$Pm\bar{3}m$	100	a = 4.007675(4)	R_p = 5.7% R_{wp} = 8.2% Chi^2 = 6.1
70	*P*4*mm*	100	a = 4.005180(7) c = 4.01067(1)	R_p = 6.0% R_{wp} = 8.7% Chi^2 = 7.0
20	*R*3*m*	57.65(4)	a = 4.006693(8) α = 89.9516(2)	R_p = 5.1% R_{wp} = 7.3%
	*P*4*mm*	42.34(5)	a = 3.999990(6) c = 4.01584(1)	Chi^2 = 4.9
-25	*R*3*m*	95.152(3)	a = 4.005129(7) α = 89.9221(1)	R_p = 4.9% R_{wp} = 7.5%
	*P*4*mm*	4.84(4)	a = 3.99516(2) c = 4.01808(6)	Chi^2 = 5.3
-100	*R*3*m*	100	a = 4.003484(8) α = 89.8956(1)	R_p = 5.7% R_{wp} = 8.3% Chi^2 = 6.3

Supplementary information to

Structure and phase transitions in $0.5(Ba_{0.7}Ca_{0.3}TiO_3)$-$0.5(BaZr_{0.2}Ti_{0.8}O_3)$ from -100 °C to 150 °C

Astri Bjørnetun Haugen,[1] Jennifer S. Forrester,[2] Dragan Damjanovic,[3] Binzhi Li,[4] Keith J. Bowman,[5] and Jacob L. Jones [2]

[1]Department of Materials Science and Engineering, Norwegian University of Science and Technology, 7491 Trondheim, Norway

[2]Department of Materials Science and Engineering, University of Florida, Gainesville, Florida 32611, USA

[3]Swiss Federal Institute of Technology – EPFL, 1015 Lausanne, Switzerland

[4]Department of Chemical Engineering and Materials Science, University of California-Davis, Davis, California 95616, USA

[5]Armour College of Engineering, Illinois Institute of Technology, Chicago, Illinois 60616, USA

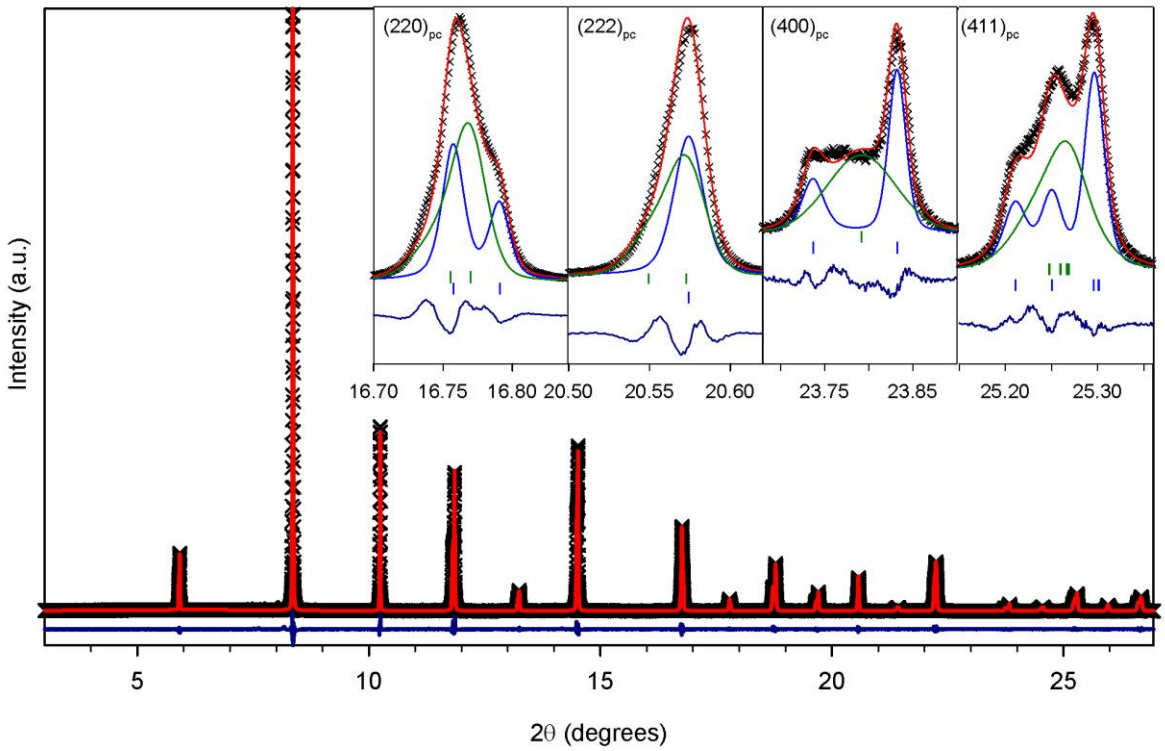

FIG. S1. The best Rietveld refinement of 50BZT-50BCT at 20 °C using mixed-phase *R*3*m* + *P*4*mm*. The contribution to scattering from both phases are shown independently.

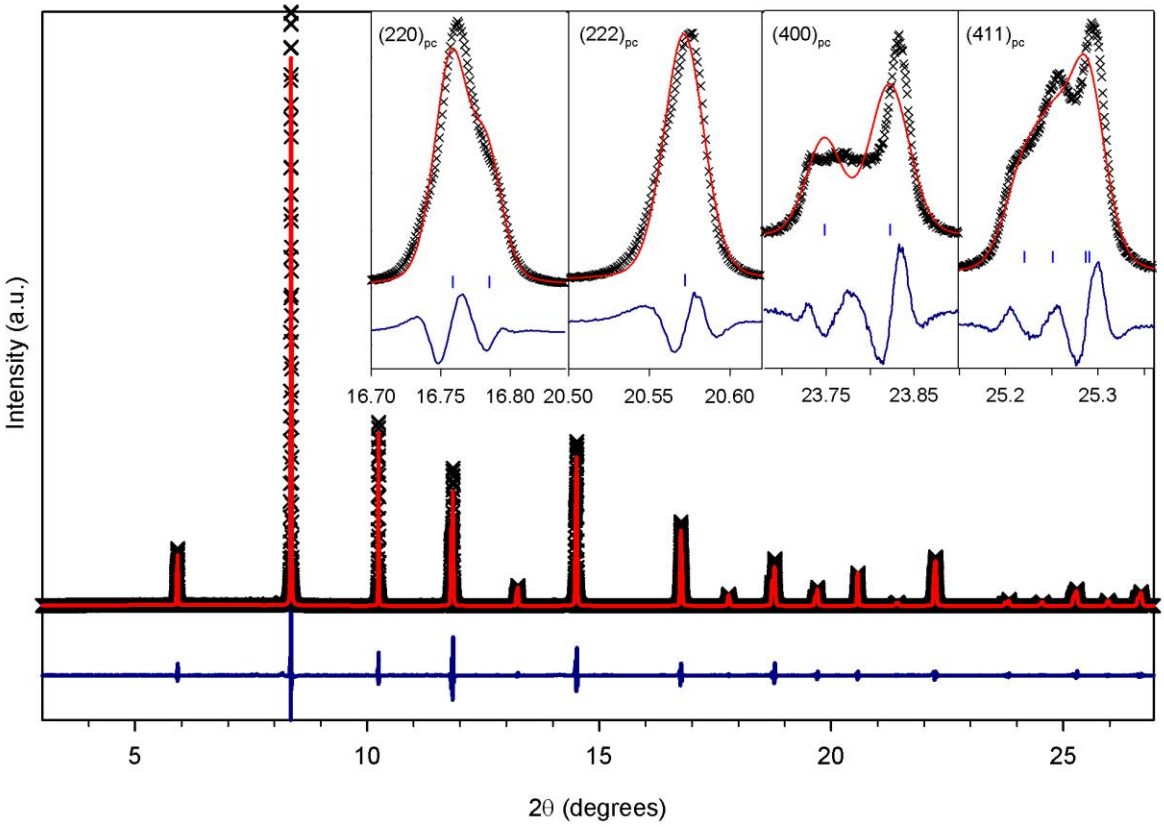

FIG. S2. The best Rietveld refinement of 50BZT-50BCT at 20 °C using *P*4*mm* only.

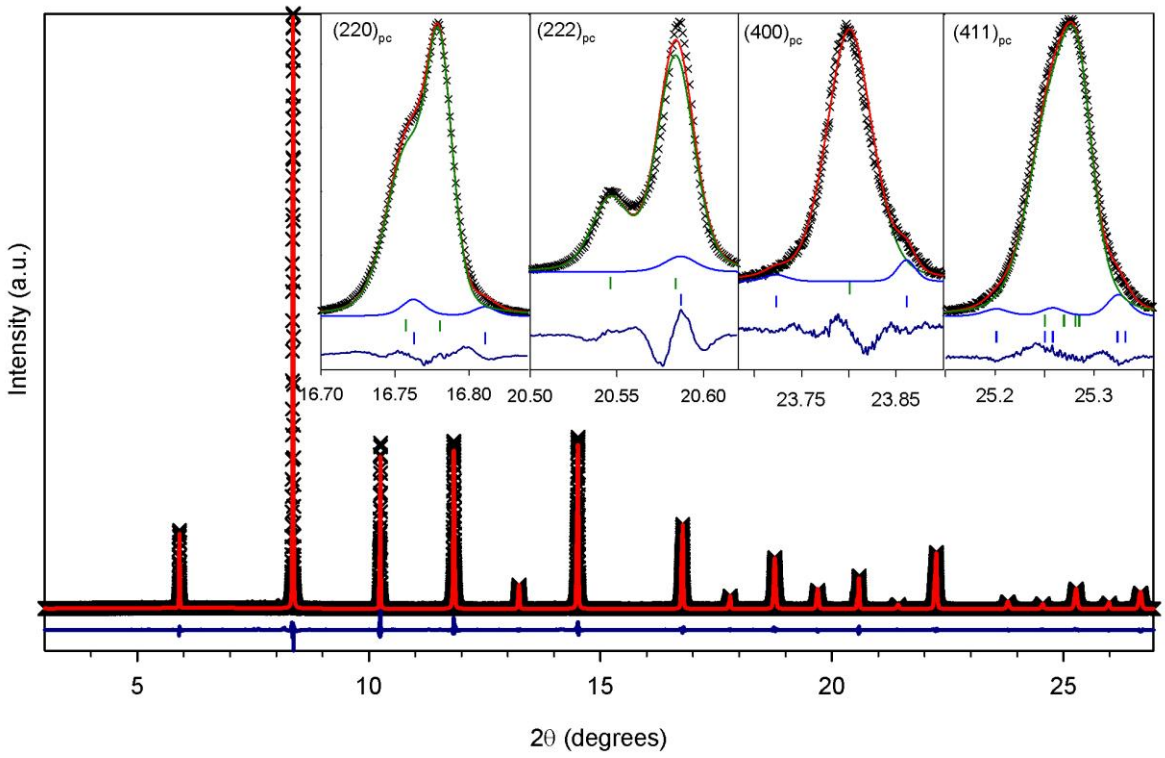

FIG. S3. The best Rietveld refinement of 50BZT-50BCT at -25 °C using mixed-phase *R*3*m* + *P*4*mm*. The contribution to scattering from both phases are shown independently.

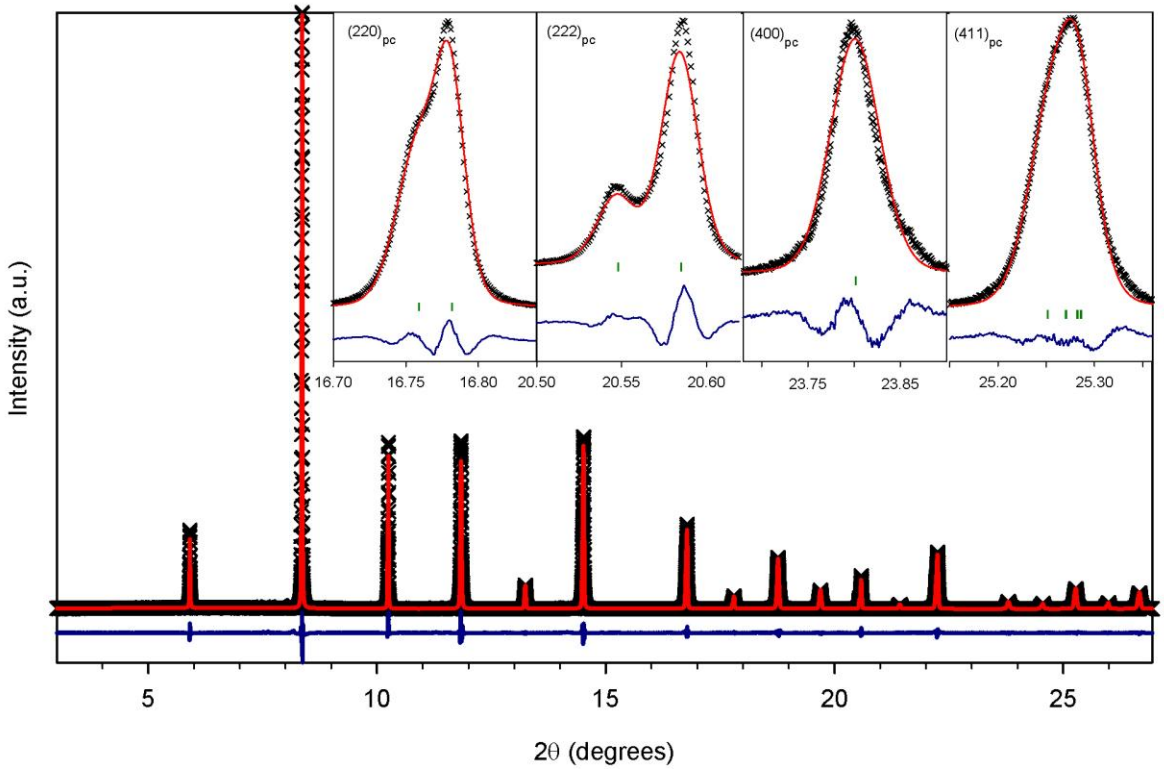

FIG. S4. The best Rietveld refinement of 50BZT-50BCT at -25 °C using *R*3*m* only.

TABLE SI. Refined parameters for 50BZT-50BCT.

Temp. (°C)	Space group		A site (Ba/Ca)	B site (Ti/Zr)	O (1)	O (2)
150	$Pm3m$	x	0	0.5	0	-
		y	0	0.5	0.5	-
		z	0	0.5	0.5	-
		U_{iso}*	0.828(6)	0.406(9)	0.98(2)	-
120	$Pm3m$	x	0	0.5	0	-
		y	0	0.5	0.5	-
		z	0	0.5	0.5	-
		U_{iso}*	0.756(5)	0.353(9)	0.92(2)	-
100	$Pm3m$	z	0	0.5	0	-
		y	0	0.5	0.5	-
		z	0	0.5	0.5	-
		U_{iso}*	0.714(6)	0.325(9)	0.88(2)	-
70	*P*4*mm*	x	0	0.5	0.5	0.5
		y	0	0.5	0.5	0
		z	0	0.499(3)	0.00(1)	0.529(2)
		U_{iso}*	0.866(6)	0.48(1)	0.6(1)	1.71(9)
20	*R*3*m*	x	0	0.502(1)	0.513(2)	-
		y	0	0.502(1)	0.513(2)	-
		z	0	0.502(1)	0.018(2)	-
		U_{iso}*	1.191(7)	0.72(2)	0.05(7)	-
	*P*4*mm*	x	0	0.5	0.5	0.5
		y	0	0.5	0.5	0
		z	0	0.494(2)	0.021(5)	0.531(2)
		U_{iso}*	0.428(7)	0.10(2)	0.8(2)	1.7(1)
-25	*R*3*m*	x	0	0.499(1)	0.508(1)	-
		y	0	0.499(1)	0.508(1)	-
		z	0	0.499(1)	0.015(3)	-
		U_{iso}*	0.706(4)	0.366(9)	0.47(3)	-
	*P*4*mm*	x	0	0.5	0.5	0.5
		y	0	0.5	0.5	0
		z	0	0.494(2)	0.021(5)	0.531(2)
		U_{iso}*	0.428(7)	0.10(2)	0.8(2)	1.7(1)
-100	*R*3*m*	x	0	0.4963(6)	0.5108(8)	-
		y	0	0.4963(6)	0.5108(8)	-
		z	0	0.4963(6)	0.0258(9)	-
		U_{iso}*	0.590(6)	0.27(1)	0.38(3)	-

*U_{iso} values are x100 Å^2